NANO LETTERS

pubs.acs.org/NanoLett Letter

Spatial Mapping of Electrostatic Fields in 2D Heterostructures

Akshay A. Murthy, Stephanie M. Ribet, Teodor K. Stanev, Pufan Liu, Kenji Watanabe, Takashi Taniguchi, Nathaniel P. Stern, Roberto dos Reis,* and Vinayak P. Dravid*

Cite This: *Nano Lett.* 2021, 21, 7131−7137 Read Online

ACCESS | Metrics & More | Article Recommendations | Supporting Information

ABSTRACT: *In situ* electron microscopy is an effective tool for understanding the mechanisms driving novel phenomena in 2D structures. However, due to practical challenges, it is difficult to address these technologically relevant 2D heterostructures with electron microscopy. Here, we use the differential phase contrast (DPC) imaging technique to build a methodology for probing local electrostatic fields during electrical operation with nanoscale spatial resolution in such materials. We find that, by combining a traditional DPC setup with a high-pass filter, we can largely eliminate electric fluctuations emanating from short-range atomic potentials. Using a method based on this filtering algorithm, *a priori* electric field expectations can be directly compared with experimentally derived values to readily identify inhomogeneities and potentially problematic regions. We use this platform to analyze the electric field and charge density distribution across layers of hBN and MoS_2.

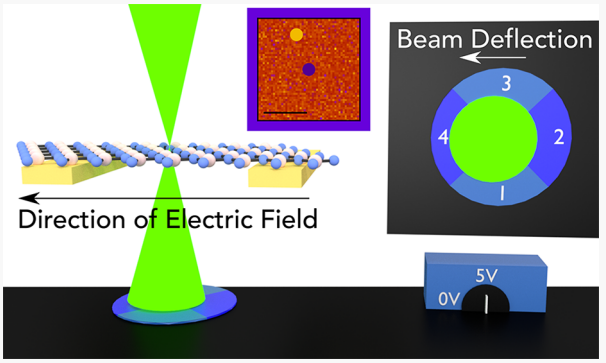

KEYWORDS: *in situ electron microscopy, heterostructure, transition-metal dichalcogenides, MoS_2, differential phase contrast*

INTRODUCTION

The diverse class of two-dimensional (2D) materials, including graphene, hexagonal boron nitride (hBN), and transition metal dichalcogenides (TMDs), has produced a wide variety of captivating and technologically relevant features for next-generation optoelectronic architectures and quantum information science.[1−3] These include unique memory devices,[4,5] Josephson junctions for solid-state qubit architectures,[6,7] photonic structures,[8−10] and electronic devices.[11−13] Although charge transport dynamics present at various 2D or contact interfaces contribute significantly to the device performance in such structures, the atomistic features giving rise to macroscopic properties often remain unclear. This makes it difficult to identify the optimal methods for improving performance and reliability thus requiring techniques combining high spatial resolution with real-time information. *In situ* electrical biasing scanning transmission electron microscopy (STEM) is a particularly attractive method for probing property−performance relationships at atomic length scales. This approach involves stimulating the sample of interest with an external electrical field while simultaneously probing it with high-energy electrons, providing sub-angstrom resolution common to STEM. It is thus possible to directly ascertain the evolution of the atomic structure with nanoscale spatial resolution, such as the electromigration of atoms in MoS_2.[14]

Moreover, causal relationships between atomistic dynamics and emergent phenomena can be most robustly defined when a single technique provides evidence of both features. STEM is particularly valuable in this context, as beyond providing conventional structural information, the multimodal nature of STEM makes it possible to concurrently detect various local phenomena. For instance, electric and/or magnetic fields within the sample partially deflect the incident electron probe, leading to shifts in the intensity center of mass (I_{COM}) in the convergent beam electron diffraction (CBED) patterns. Methods such as differential phase contrast (DPC) facilitate the measurement of such beam−specimen interactions.[15−17] Traditional DPC relies on physical, segmented detectors symmetrically positioned about the optic axis. Measuring differences in the electron signal intensity between opposite segments in the diffraction plane provides information associated with the deflection that the electron probe experiences along the common detector axis.[18−21]

The advent of high-speed direct detection cameras, which can capture the scattered electron probe at each pixel in a real-space image with roughly 10^{-3} s dwell times,[22,23] has popularized the use of virtual segmented detectors as an alternative option for DPC measurement. In this method, binary filters are applied to each recorded CBED pattern in order to measure a CBED signal falling within a specified

Received: April 25, 2021
Revised: August 19, 2021
Published: August 27, 2021

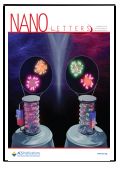

segmented area. Further, these cameras have enabled DPC measurements based on first moment (FM)-STEM detection schemes. In this case, a summation of the measured intensities at each detector pixel allows for the direct calculation of the I_{COM} value, thereby providing microscopists with many options for extracting electronic and magnetic field information.[24,25]

Here we investigate 2D layers that can be simultaneously stimulated with external electrical potential while they are probed with an electron beam (Figure 1). Using DPC measurements to calculate variations in the I_{COM} value of the electron probe, we are able to map the electrostatic fields and charge densities that arise in 2D layers when an external potential is present. Additionally, we demonstrate the capability to selectively amplify low spatial frequency information associated with these long-range potentials by employing virtual annular segmented detectors. This method provides ample opportunities for critical investigations of other systems, including a wide variety of 2D memory, quantum, and optoelectronic heterostructure devices.

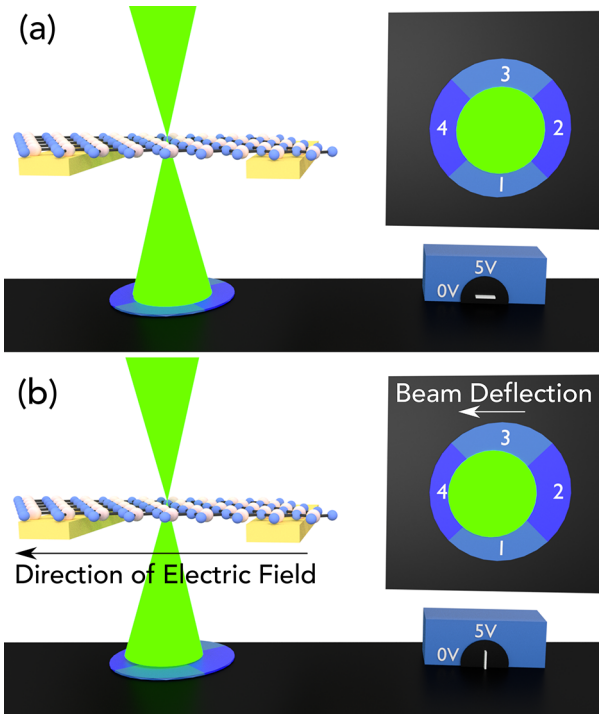

Figure 1. Schematic of STEM electrical field measurement setup (a) prior to applying an external electrical potential and (b) while applying an external electrical potential. This external potential leads to a deflection in the center of mass of the electron diffraction pattern.

RESULTS AND DISCUSSION

Although fabricating TEM devices of 2D materials and heterostructures is typically a challenging task, the construction of such structures is feasible through a process we introduced previously.[14] In this method, 75 nm thick gold electrodes are patterned using electron beam lithography on a SiO_2/Si (300 nm thickness) substrate. This substrate is then spin-coated with a polycarbonate solution (5% polycarbonate/95% chloroform w/v) at 2000 rpm for 60 s. After this coating is baked at 120 °C for 1 min, the substrate is placed in DI water until the polymer containing the gold electrodes is released naturally from the substrate. After the polymer film is dried, it is carefully placed on two strips of PDMS gel attached to a glass slide and suspended roughly 1 mm above the glass slide. Using a micromanipulator stage, the gold electrodes are aligned over a TEM window (TEMwindows.com) and brought into contact with the TEM grid. This assembly is then gradually heated to 150 °C for a few minutes before the sample is baked at 170 °C for 15 min. The structure is then placed in a chloroform bath for 6 h to dissolve the polycarbonate film and moved to an IPA bath afterward for a few minutes to remove chloroform residue.

Once a thin layer of mechanically exfoliated hBN (Figure S1) or a mechanically transferred MoS_2/hBN heterostructure is identified on a SiO_2/Si substrate, a similar process is then repeated to move the 2D layers from the substrate to the TEM grid. The resultant sample is left overnight in chloroform and moved to an IPA bath afterward. The sample is then annealed in a 95% Ar/5% H_2 mixture at 200 °C for 2 h to remove residue prior to STEM imaging. Finally, gold wires are used to connect the electrode pads to the contact points on the Nanofactory TEM holder using indium as a bonding agent. Following fabrication of the sample, Raman and photoluminescence (PL) spectra are taken to confirm the presence of suspended layers of MoS_2 and hBN (Figure S2). The current−voltage characteristics that arise when a voltage is applied across this sample is provided in Figure S2, demonstrating the ability to apply an external field across the sample.

S/TEM images of 2D layers are acquired using a JEOL ARM 300F Grand ARM S/TEM operated at 300 kV. The camera length is set to 8 cm, and the condenser aperture is selected to provide a convergence semiangle of 30 mrad with a beam current of 20 pA in order to minimize beam-induced damage. A large convergence semiangle (30 mrad) is intentionally selected to maximize the spatial resolution.[26] A 4D STEM data set containing over 40000 CBED patterns is acquired in a 680 × 80 mesh (pixel size of 5.96 Å) across the sample using a Gatan K3-IS camera in counting mode. A frame rate of 285 fps (0.0035 s per diffraction) is chosen to prioritize acquisition of high-resolution CBED (1024 × 1024 pixels) while sufficient sample stability is maintained under an external bias.

Intensity variations in the CBED pattern can be related to in-plane electric fields. When an electric field is present in the sample plane, the incident beam of electrons experiences a Coulombic force, leading to a displacement in the CBED pattern parallel to the detector axis. As discussed, there exist multiple DPC methods to measure these changes in the I_{COM} value of the CBED pattern as a function of position. The I_{COM} values calculated at each probe position can be related to the expectation value of the momentum transfer, $\langle p_\perp \rangle$, by rearranging de Broglie's wave equation and normalizing the overall electron probe intensity (eq 1). In this equation, h represents Planck's constant and λ represents the electron wavelength.

$$\langle p_\perp \rangle = h\frac{\sin I_{COM}}{\lambda} \quad (1)$$

Further, Müller et al. showed that, on the basis of Ehrenfest's theorem, the measured in-plane electric field is given by eq 2.[27] In this equation, v represents the velocity of electrons carrying a charge e that interact with the sample for a time equal to v/z, where z represents the thickness of the sample.[27,28]

https://doi.org/10.1021/acs.nanolett.1c01636
Nano Lett. 2021, 21, 7131−7137

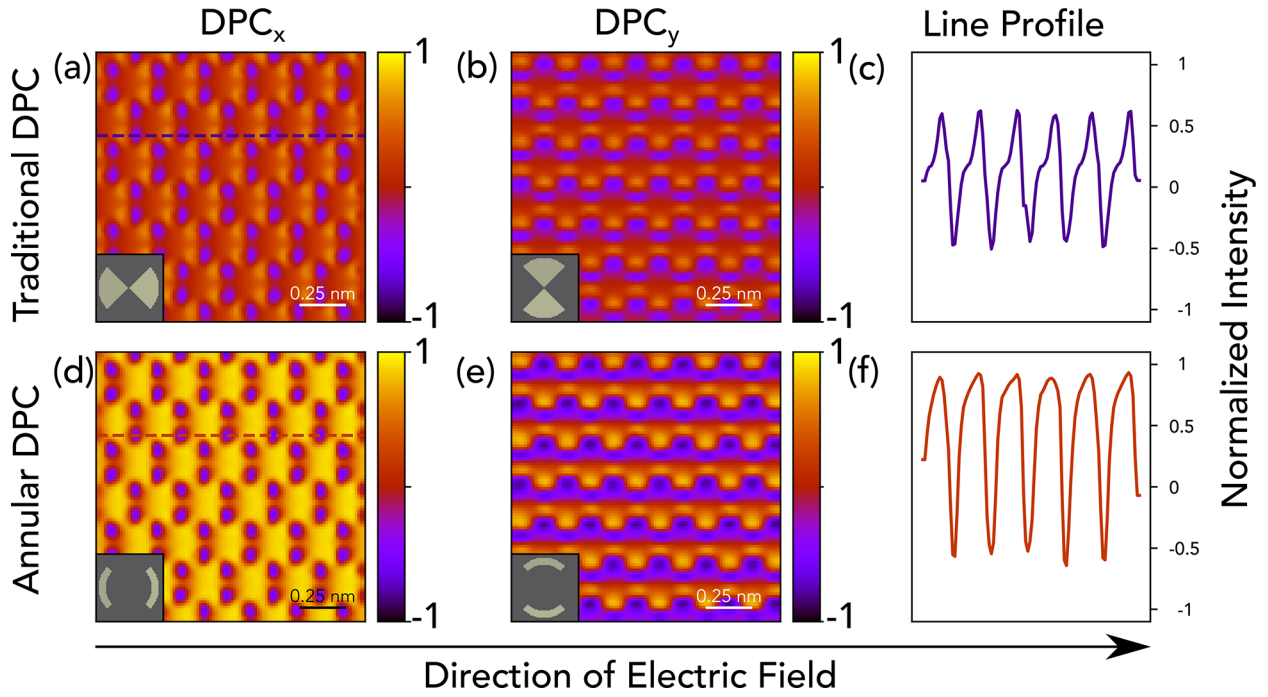

Figure 2. DPC simulations for interrogating long-range electric fields: (a, b) simulated DPC images taken from the hBN structure subjected to a linear gradient in the electrical potential in the horizontal direction detailed in Figure S4 with detector configurations provided in the insets; (c) intensity line profile taken from (a); (d, e) simulated annular DPC images taken from the same hBN structure with detector configurations provided in the insets; (f) intensity line profile taken from (d). From these line profiles, the simulated data suggest that intensity shifts from long-range electric fields are significantly enhanced in the annular geometry.

$$E_{\perp} = \langle p_{\perp} \rangle \frac{v}{ez} \tag{2}$$

Because this equation assumes that the intensity of the electron probe does not vary with z, this relation does, however, require specimen thicknesses to be restricted to values of less than 5 nm, such as the 2D samples examined here, in order to avoid beam-broadening effects.[27,29] In the case of thicker samples, sources of diffraction contrast can also contribute to probe deflection and introduce imaging artifacts.[30]

With respect to the underlying nature of deflections in the I_{COM} value, Cao et al. previously provided evidence that fields exhibiting low spatial frequencies (i.e., long-range fields) generate a uniform displacement of the CBED pattern.[31] Meanwhile, fields exhibiting high spatial frequencies (i.e., short-range fields) produce a redistribution in intensity within the CBED pattern.[31] As such, one method to amplify information associated with long-range fields is through the use of an annular DPC detector.[32] In such a segmented detector, when the inner collection semiangle approaches the convergence semiangle of the CBED pattern, the effect of redistribution in a signal associated with short-range potentials is largely reduced. Simulated differential phase contrast images of hBN subjected to an external electric field demonstrate this aspect (Figure 2 and Figure S5). In the case of a traditional DPC image (Figure 2a,b), short-range atomic electrostatic potentials and long-range external potentials both contribute to the measured signal. As discussed by Nguyen et al., in annular DPC images, however (parameters given in Methods), the contribution of local potentials is selectively diminished (line profiles provided in Figure 2c,f).[33] Thus, we apply this method to better visualize long-range electric fields. In comparison to alternative techniques outlined by Krajnak et al.[34] and Müller-Caspary et al.,[35] the method applied here is computationally inexpensive, is extendable to a variety of material systems, and does not significantly degrade spatial resolution.

Experimental results displaying I_{COM} values measured in a layer of hBN prior to applying and while applying an external electrical potential are presented in Figure 3. Prior to application of this external potential, the CBED pattern taken from spot 1 on the TEM image is provided in Figure 3a. The center portion of individual CBED patterns is provided in Figure 3b in order to better observe the beam deflections present in these diffraction patterns. The purple dots represent the I_{COM} values of the vacuum probe that has not interacted with the sample in these electron diffraction patterns. Meanwhile, the yellow dots represent the I_{COM} values of the CBED pattern taken from the specified positions of the hBN layer. Virtual quadrant segmented detectors are used to calculate these I_{COM} values. When this measurement is repeated in the case where an external voltage of 5 V is applied and a long-range electric field arises in the direction of the indicated arrow (Figure 3c), larger deflections in the I_{COM} values in comparison to the vacuum probe are present. This indicates that the external electric field leads to the incident electron probe experiencing additional momentum transfer.

A monolayer of MoS_2 is placed on top of the hBN layers using the previously defined sample preparation process to produce a more electronically relevant structure. This semiconducting layer provides an alternative current pathway, and this architecture represents a tunneling contact geometry previously explored for reducing contact resistance.[36,37] Once more, it is apparent that applying an external voltage leads to greater beam deflection in this geometry (Figure 3d–f).

Equation 2 is applied to relate shifts in the I_{COM} value of the CBED pattern to the electric field distribution. In the absence

https://doi.org/10.1021/acs.nanolett.1c01636
Nano Lett. 2021, 21, 7131−7137

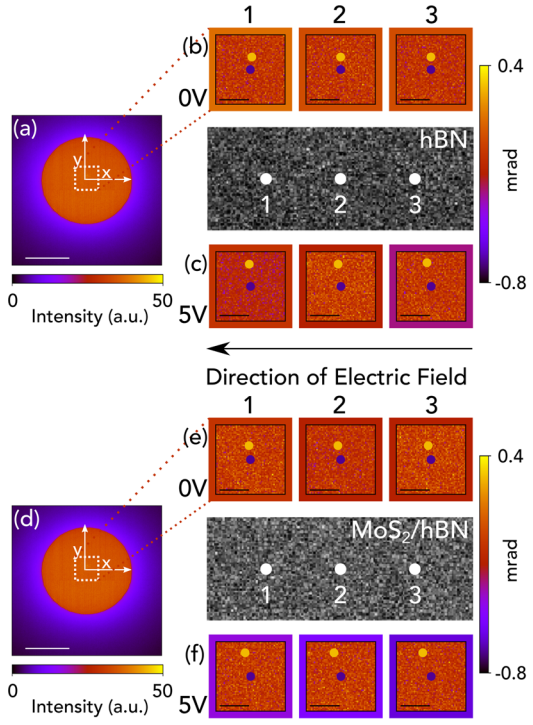

Figure 3. Experimental scanning diffraction data acquired from the sample seen in the center dark field TEM image. (a) CBED patterns captured at point 1 marked on the hBN sample. The color bar intensity is in units of relative detection intensity. CBED patterns taken as a function of indicated positions when (b) 0 V and (c) 5 V are applied to the hBN sample. The purple dots refer to the center of mass of the CBED pattern taken from regions devoid of sample, while the yellow dots represent the center of mass of the CBED pattern taken from a particular position. The border color represents the degree of probe deflection in the x direction. (d) CBED patterns captured at point 1 marked on the MoS_2/hBN sample. The color bar intensity is in units of relative detection intensity. CBED patterns taken as a function of indicated positions when (e) 0 V and (f) 5 V are applied to the MoS_2/hBN sample. Scale bars in (a) and (d) represent 30 mrad, and scale bars in (b), (c), (e), and (f) represent 2 mrad. A clear shift in the center of mass is observed when an external field is applied for both samples.

of an external electric field, the relative orientation and magnitude of the measured fields are seen in Figure 4. The noisy pattern observed (Figure 4a) likely represents the interaction between atomic orbitals in the sample and the electron probe.[27]

In order to calculate the electric field distribution when an external voltage of 5 V is applied, electrons detected at each probe position are filtered using a virtual quadrant annular segmented detector (Methods). Once again, the electric field vector at each probe position is calculated using eq 2. A map of the relative electric field distribution when an external voltage of 5 V is applied is provided in Figure 4b. The calculated field using the annular detector architecture agrees with our expectations for the uniform field distribution that would arise when this uniform electrical field is applied across hBN.

For the MoS_2/hBN sample, similar methods are used to characterize the resultant relative electrical fields in the absence of an external voltage and the long-range fields that arise when an external electric field is applied. These, too, agree with prior expectations, as they are indicative of a uniform long-range field existing across the sample (Figure 4c,d).

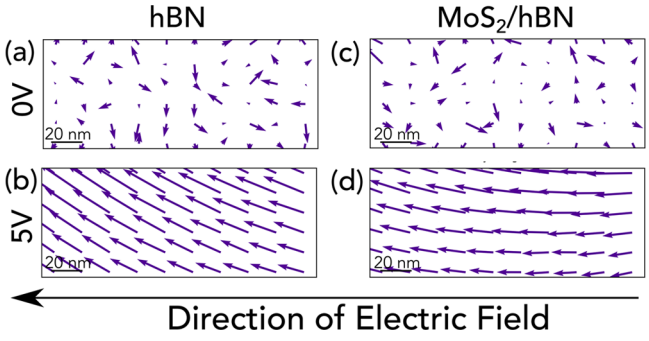

Figure 4. Experimental relative electric field maps. In the absence of an applied bias, electric field maps of the (a) hBN and (c) MoS_2/hBN samples are provided. Similar field maps in the case where an external bias of 5 V is applied are provided for the (b) hBN and (d) MoS_2/hBN samples, respectively. In the case of an applied field, the measured electric field vectors align with the external potential gradient.

Due to the need for additional theoretical explorations regarding quantification of the annular DPC signal, we have provided relative electric field maps in this work. Further, the measured electric field includes contributions from the electrostatic field in the sample plane as well as the leakage electric fields in the vacuum regions directly above and beneath the sample. We model the relative intensity of this leakage field by solving Laplace's equation for the sample geometry, as seen in Figure S8. These calculations suggest that while the accumulated leakage field scales with the sample field, it can persist for several hundred nanometers both above and beneath the sample. As such, a rigorous analysis of the size of the electric field would be needed to quantitatively extract the precise electric field magnitudes within the sample, which is outside the scope of this study.

Finally, since Maxwell's theory states that the divergence of the electric field is proportional to the charge density (Methods), a relative charge density distribution of the MoS_2/hBN region when an electric field is present is provided in Figure S9. From this figure, it appears that the heterostructure is free of any charge discontinuities within the structure.

CONCLUDING REMARKS

In summary, we demonstrate the ability to measure the electrostatic field distribution that arises in 2D materials as a function of applied electric field. This technique involves the use of an annular DPC mask to relate shifts in the center of mass of the CBED pattern as a function of position to local fields. Through simulated and experimental investigations, we determine that such masks provide a method for selectively amplifying the low spatial frequency information associated with long-range electric fields. This work demonstrates that, moving forward, these tools offer both a route to identifying nonuniformities in the electric field and potential sources of noise or performance degradation during device operation in 2D architectures.

METHODS

Material Synthesis. Single-crystal flakes of monolayer MoS_2 were grown through an atmospheric pressure chemical vapor deposition process (CVD). This process involved the use of 5 mg of MoO_3 (Sigma-Aldrich) powder, which was

https://doi.org/10.1021/acs.nanolett.1c01636
Nano Lett. 2021, 21, 7131−7137

spread evenly throughout an alumina boat and capped by two face-down, 1 cm by 1 cm SiO_2/Si substrates (300 nm oxide). This boat was placed within a 1 in. diameter quartz tube at the center of a tube furnace. Similarly, 300 mg of sulfur pieces (Alfa-Aesar) was placed in another alumina boat located upstream and outside of the furnace. Following a 15 min purge of the sealed quartz tube with argon gas, the center of the furnace was heated to 700 °C over a period of 40 min and held at that temperature for 3 min. During this process, the flow rate of argon gas was maintained at 13 standard cubic centimeters per minute. When the temperature of the furnace reached 575 °C during this ramp step, the alumina boat containing the sulfur was moved to a region inside the furnace where the temperature was approximately 150 °C. This was done with the help of a magnet. Following the growth process, the furnace was allowed to cool naturally.

DPC STEM Simulations. Multislice simulations were performed using custom MATLAB codes following the methods laid out by Kirkland.[38] These simulations used microscope parameters similar to those used in acquiring the experimental datasets along with eight frozen phonon configurations. An external potential was applied by adding a mesh grid with linearly varying potentials from 0 to 10 kV to the first layer of the multislice calculation. Traditional DPC images were acquired by processing the data using the virtual quadrant detectors seen in Figure 2. Electron signals in quadrants parallel to the x-axis were subtracted from one another to acquire DPC_x images, and electron signals in quadrants parallelto the y-axis were subtracted from one another to acquire DPC_y images. For annular DPC images, the data were processed using the virtual annular quadrant detectors seen in Figure 2 with an inner collection semiangle of 28 mrad and an outer collection semiangle of 32 mrad. DPC_x and DPC_y images were acquired through similar means.

Scanning Diffraction Image Processing. 4D STEM data sets were processed using custom Python scripts. For the analysis associated with samples under no applied bias, the x and y components of the intensity center of mass at each probe position (I_{COM}) were calculated using a traditional quadrant detector. For the analysis associated with samples under an applied bias, the transmitted electron signal both prior to application and after application of applied bias was filtered using an annular quadrant detector. This virtual DPC detector was constructed to have an inner collection semiangle of 28 mrad and an outer collection semiangle of 32 mrad. The measured signal in the x and y annular quadrants is used to approximate the x and y components of the I_{COM} value.

Following the protocol detailed by Fang et al. and Müller et al.,[27,39] electric field maps were calculated using the x and y components of the I_{COM} values. These values were related to the expectation value of the momentum transfer, $\langle p_\perp \rangle$, through eq 1. $\langle p_\perp \rangle$ is calculated in units of eV s Å^{-1}. Equation 2 was used to relate the expectation value of the momentum transfer to the electric field. $E_\perp$ is represented in the text using a quiver plot displaying both the E_x and E_y components.

The total charge density (ρ), which is represented in units of elementary charge per Å^2, was calculated using eq 3. In this equation, ε_0 represents the vacuum permittivity.

$$\mathrm{div}(E_\perp z) = \frac{\rho}{\varepsilon_0} \tag{3}$$

Confocal Raman Spectroscopy. Raman spectra were obtained using a Horiba LabRAM HR Evolution confocal Raman system under laser illumination with a wavelength of 532 nm and a power of 0.25 mW.

■ ASSOCIATED CONTENT

Supporting Information

The Supporting Information is available free of charge at https://pubs.acs.org/doi/10.1021/acs.nanolett.1c01636.

Height profile of thin hBN support layers, spectroscopy and current−voltage characteristics from the prepared TEM sample, additional simulated data using annular DPC detectors, TEM diffraction pattern taken from the MoS_2/hBN sample, leakage field simulations, and charge density maps across MoS_2/hBN (PDF)

■ AUTHOR INFORMATION

Corresponding Authors

Roberto dos Reis − *Department of Materials Science and Engineering, Northwestern University, Evanston, Illinois 60208, United States; The NUANCE Center, Northwestern University, Evanston, Illinois 60208, United States;* Email: roberto.reis@northwestern.edu

Vinayak P. Dravid − *Department of Materials Science and Engineering, Northwestern University, Evanston, Illinois 60208, United States; The NUANCE Center and International Institute of Nanotechnology, Northwestern University, Evanston, Illinois 60208, United States;* orcid.org/0000-0002-6007-3063; Email: v-dravid@northwestern.edu

Authors

Akshay A. Murthy − *Department of Materials Science and Engineering, Northwestern University, Evanston, Illinois 60208, United States; International Institute of Nanotechnology, Northwestern University, Evanston, Illinois 60208, United States;* Present Address: Superconducting Quantum Materials and Systems (SQMS) Division, Fermi National Accelerator Laboratory, Batavia, Illinois 60510, United States; orcid.org/0000-0001-7677-6866

Stephanie M. Ribet − *Department of Materials Science and Engineering, Northwestern University, Evanston, Illinois 60208, United States; International Institute of Nanotechnology, Northwestern University, Evanston, Illinois 60208, United States*

Teodor K. Stanev − *Department of Physics and Astronomy, Northwestern University, Evanston, Illinois 60208, United States*

Pufan Liu − *Department of Materials Science and Engineering, Northwestern University, Evanston, Illinois 60208, United States*

Kenji Watanabe − *Research Center for Functional Materials, National Institute for Materials Science, Tsukuba 305-0044, Japan;* orcid.org/0000-0003-3701-8119

Takashi Taniguchi − *International Center for Materials Nanoarchitectonics, National Institute for Materials Science, Tsukuba 305-0044, Japan;* orcid.org/0000-0002-1467-3105

Nathaniel P. Stern − *Department of Physics and Astronomy, Northwestern University, Evanston, Illinois 60208, United States;* orcid.org/0000-0002-8903-3516

Complete contact information is available at:

https://doi.org/10.1021/acs.nanolett.1c01636
Nano Lett. 2021, 21, 7131−7137

https://pubs.acs.org/10.1021/acs.nanolett.1c01636

Author Contributions

The manuscript was written through contributions of all authors. All authors have given approval to the final version of the manuscript.

Notes

The authors declare no competing financial interest.

■ ACKNOWLEDGMENTS

This material is based upon work supported by the National Science Foundation under Grant No. DMR-1929356. This work made use of the EPIC, Keck-II, and SPID facilities of Northwestern University's NUANCE Center, which has received support from the SHyNE Resource (NSF ECCS-2025633), the IIN, and Northwestern's MRSEC program (NSF DMR-1720139). A.A.M. and S.M.R. gratefully acknowledge support from the Ryan Fellowship and the IIN at Northwestern University. T.K.S. was supported by the Office of Naval Research (N00014-16-1-3055) and the National Science Foundation (DMR-1905986). P.L. was supported by Argonne National Laboratory. K.W. and T.T. acknowledge support from the Elemental Strategy Initiative conducted by the MEXT, Japan, Grant No. JPMXP0112101001, JSPS KAKENHI Grant No. JP20H00354 and the CREST (JPMJCR15F3), JST. The authors thank Erik Lenferink for assistance with sample characterization. Research reported in this publication was supported in part by instrumentation provided by the Office of The Director, National Institutes of Health, of the National Institutes of Health under Award No. S10OD026871. The content is solely the responsibility of the authors and does not necessarily represent the official views of the National Institutes of Health. This research was supported in part through the computational resources and staff contributions provided for the Quest high-performance computing facility at Northwestern University, which is jointly supported by the Office of the Provost, the Office for Research, and Northwestern University Information Technology.

■ REFERENCES

(1) Cho, B.; Yoon, J.; Lim, S. K.; Kim, A. R.; Kim, D.-H.; Park, S.-G.; Kwon, J.-D.; Lee, Y.-J.; Lee, K.-H.; Lee, B. H.; Ko, H. C.; Hahm, M. G. Chemical Sensing of 2D Graphene/MoS_2 Heterostructure Device. *ACS Appl. Mater. Interfaces* **2015**, *7*, 16775−16780.

(2) Yang, Y.; Fei, H.; Ruan, G.; Xiang, C.; Tour, J. M. Edge-Oriented MoS_2 Nanoporous Films as Flexible Electrodes for Hydrogen Evolution Reactions and Supercapacitor Devices. *Adv. Mater.* **2014**, *26*, 8163−8168.

(3) Jiang, J.; Guo, J.; Wan, X.; Yang, Y.; Xie, H.; Niu, D.; Yang, J.; He, J.; Gao, Y.; Wan, Q. 2D MoS_2 Neuromorphic Devices for Brain-Like Computational Systems. *Small* **2017**, *13*, 1700933.

(4) Luo, Y. K.; Xu, J.; Zhu, T.; Wu, G.; McCormick, E. J.; Zhan, W.; Neupane, M. R.; Kawakami, R. K. Opto-Valleytronic Spin Injection in Monolayer MoS_2/Few-Layer Graphene Hybrid Spin Valves. *Nano Lett.* **2017**, *17*, 3877−3883.

(5) Ge, R.; Wu, X.; Kim, M.; Shi, J.; Sonde, S.; Tao, L.; Zhang, Y.; Lee, J. C.; Akinwande, D. Atomristor: Nonvolatile Resistance Switching in Atomic Sheets of Transition Metal Dichalcogenides. *Nano Lett.* **2018**, *18*, 434−441.

(6) Calado, V. E.; Goswami, S.; Nanda, G.; Diez, M.; Akhmerov, A. R.; Watanabe, K.; Taniguchi, T.; Klapwijk, T. M.; Vandersypen, L. M. Ballistic Josephson Junctions in Edge-Contacted Graphene. *Nat. Nanotechnol.* **2015**, *10*, 761−4.

(7) Kim, M.; Park, G. H.; Lee, J.; Lee, J. H.; Park, J.; Lee, H.; Lee, G. H.; Lee, H. J. Strong Proximity Josephson Coupling in Vertically Stacked $NbSe_2$-Graphene-$NbSe_2$ Van Der Waals Junctions. *Nano Lett.* **2017**, *17*, 6125−6130.

(8) Wang, F.; Wang, Z.; Xu, K.; Wang, F.; Wang, Q.; Huang, Y.; Yin, L.; He, J. Tunable GaTe-MoS_2 Van Der Waals P−N Junctions With Novel Optoelectronic Performance. *Nano Lett.* **2015**, *15*, 7558−7566.

(9) Wu, W.; Wang, L.; Yu, R.; Liu, Y.; Wei, S.-H.; Hone, J.; Wang, Z. L. Piezophototronic Effect in Single-Atomic-Layer MoS_2 for Strain-Gated Flexible Optoelectronics. *Adv. Mater.* **2016**, *28*, 8463−8468.

(10) Choi, M. S.; Qu, D.; Lee, D.; Liu, X.; Watanabe, K.; Taniguchi, T.; Yoo, W. J. Lateral MoS_2 P−N Junction Formed by Chemical Doping for Use in High-Performance Optoelectronics. *ACS Nano* **2014**, *8*, 9332−9340.

(11) Late, D. J.; Liu, B.; Matte, H. R.; Dravid, V. P.; Rao, C. Hysteresis in Single-Layer MoS_2 Field Effect Transistors. *ACS Nano* **2012**, *6*, 5635−5641.

(12) Wang, J.; Yao, Q.; Huang, C.; Zou, X.; Liao, L.; Chen, S.; Fan, Z.; Zhang, K.; Wu, W.; Xiao, X.; et al. High Mobility MoS_2 Transistor With Low Schottky Barrier Contact by Using Atomic Thick H-BN as a Tunneling Layer. *Adv. Mater.* **2016**, *28*, 8302−8308.

(13) Liu, X.; Qu, D.; Ryu, J.; Ahmed, F.; Yang, Z.; Lee, D.; Yoo, W. J. P-Type Polar Transition of Chemically Doped Multilayer MoS_2 Transistor. *Adv. Mater.* **2016**, *28*, 2345−2351.

(14) Murthy, A. A.; Stanev, T. K.; Dos Reis, R.; Hao, S.; Wolverton, C.; Stern, N. P.; Dravid, V. P. Direct Visualization of Electric-Field-Induced Structural Dynamics in Monolayer Transition Metal Dichalcogenides. *ACS Nano* **2020**, *14*, 1569−1576.

(15) Rose, H. Nonstandard Imaging Methods in Electron Microscopy. *Ultramicroscopy* **1976**, *2*, 251−267.

(16) Rose, H. Image Formation by Inelastically Scattered Electrons in Electron Microscopy. *Optik* **1976**, *45*, 139−158.

(17) Dekkers, N. H.; Lang, H. D. Differential Phase-Contrast in a STEM. *Optik* **1974**, *41*, 452−456.

(18) Shibata, N.; Findlay, S. D.; Kohno, Y.; Sawada, H.; Kondo, Y.; Ikuhara, Y. Differential Phase-Contrast Microscopy at Atomic Resolution. *Nat. Phys.* **2012**, *8*, 611−615.

(19) Chapman, J. N.; Batson, P. E.; Waddell, E. M.; Ferrier, R. P. The Direct Determination of Magnetic Domain Wall Profiles by Differential Phase Contrast Electron Microscopy. *Ultramicroscopy* **1978**, *3*, 203−14.

(20) Waddell, E. M.; Chapman, J. N. Linear Imaging of Strong Phase Objects Using Asymmetrical Detectors in STEM. *Optik* **1979**, *54*, 452−456.

(21) Close, R.; Chen, Z.; Shibata, N.; Findlay, S. D. Towards Quantitative, Atomic-Resolution Reconstruction of the Electrostatic Potential via Differential Phase Contrast Using Electrons. *Ultramicroscopy* **2015**, *159*, 124−137.

(22) Battaglia, M.; Contarato, D.; Denes, P.; Giubilato, P. Cluster Imaging With a Direct Detection CMOS Pixel Sensor in Transmission Electron Microscopy. *Nucl. Instrum. Methods Phys. Res., Sect. A* **2009**, *608*, 363−365.

(23) Ophus, C. Four-Dimensional Scanning Transmission Electron Microscopy (4d-Stem): From Scanning Nanodiffraction to Ptychography and Beyond. *Microsc. Microanal.* **2019**, *25*, 563−582.

(24) Müller-Caspary, K.; Krause, F. F.; Winkler, F.; Beche, A.; Verbeeck, J.; Van Aert, S.; Rosenauer, A. Comparison of First Moment STEM With Conventional Differential Phase Contrast and the Dependence on Electron Dose. *Ultramicroscopy* **2019**, *203*, 95−104.

(25) Lazić, I.; Bosch, E. G. T.; Lazar, S. Phase Contrast STEM for Thin Samples: Integrated Differential Phase Contrast. *Ultramicroscopy* **2016**, *160*, 265−280.

(26) Lee, G.; Jeong, J.; Schwarzhuber, F.; Zweck, J.; Kim, J.; Kim, D. H.; Chang, H. J. Influence of combinatory effects of STEM setups on the sensitivity of differential phase contrast imaging. *Micron* **2019**, *127*, 102755.

(27) Müller, K.; Krause, F. F.; Béché, A.; Schowalter, M.; Galioit, V.; Löffler, S.; Verbeeck, J.; Zweck, J.; Schattschneider, P.; Rosenauer, A. Atomic Electric Fields Revealed by a Quantum Mechanical Approach to Electron Picodiffraction. *Nat. Commun.* **2014**, *5*, 5653.

(28) Seki, T.; Sánchez-Santolino, G.; Ishikawa, R.; Findlay, S. D.; Ikuhara, Y.; Shibata, N. Quantitative electric field mapping in thin specimens using a segmented detector: Revisiting the transfer function for differential phase contrast. *Ultramicroscopy* **2017**, *182*, 258−263.
(29) Müller-Caspary, K.; Krause, F. F.; Grieb, T.; Löffler, S.; Schowalter, M.; Béché, A.; Galioit, V.; Marquardt, D.; Zweck, J.; Schattschneider, P.; Verbeeck, J.; Rosenauer, A. Measurement of atomic electric fields and charge densities from average momentum transfers using scanning transmission electron microscopy. *Ultramicroscopy* **2017**, *178*, 62−80.
(30) MacLaren, I.; Wang, L.; McGrouther, D.; Craven, A. J.; McVitie, S.; Schierholz, R.; Kovács, A.; Barthel, J.; Dunin-Borkowski, R. E. On the origin of differential phase contrast at a locally charged and globally charge-compensated domain boundary in a polar-ordered material. *Ultramicroscopy* **2015**, *154*, 57−63.
(31) Cao, M. C.; Han, Y.; Chen, Z.; Jiang, Y.; Nguyen, K. X.; Turgut, E.; Fuchs, G. D.; Muller, D. A. Theory and practice of electron diffraction from single atoms and extended objects using an EMPAD. *Microscopy* **2018**, *67*, i150−i161.
(32) Chapman, J. N.; McFadyen, I. R.; McVitie, S. Modified differential phase contrast Lorentz microscopy for improved imaging of magnetic structures. *IEEE Trans. Magn.* **1990**, *26*, 1506−1511.
(33) Nguyen, K. X.; Turgut, E.; Cao, M. C.; Glaser, J.; Chen, Z.; Stolt, M. J.; Jin, S.; Fuchs, G. D.; Muller, D. A. *Disentangling magnetic and grain contrast in polycrystalline FeGe thin films using 4-D Lorentz Scanning Transmission Electron Microscopy*. arXiv preprint arXiv:2001.06900, 2020.
(34) Krajnak, M.; McGrouther, D.; Maneuski, D.; Shea, V. O.; McVitie, S. Pixelated detectors and improved efficiency for magnetic imaging in STEM differential phase contrast. *Ultramicroscopy* **2016**, *165*, 42−50.
(35) Müller-Caspary, K.; Grieb, T.; Müßener, J.; Gauquelin, N.; Hille, P.; Schörmann, J.; Verbeeck, J.; Van Aert, S.; Eickhoff, M.; Rosenauer, A. Electrical Polarization in AlN/GaN Nanodisks Measured by Momentum-Resolved 4D Scanning Transmission Electron Microscopy. *Phys. Rev. Lett.* **2019**, *122*, 106102.
(36) Murthy, A. A.; Stanev, T. K.; Cain, J. D.; Hao, S.; LaMountain, T.; Kim, S.; Speiser, N.; Watanabe, K.; Taniguchi, T.; Wolverton, C.; Stern, N. P.; Dravid, V. P. Intrinsic Transport in 2D Heterostructures Mediated Through H-Bn Tunneling Contacts. *Nano Lett.* **2018**, *18*, 2990−2998.
(37) Chandni, U.; Watanabe, K.; Taniguchi, T.; Eisenstein, J. P. Evidence for Defect-Mediated Tunneling in Hexagonal Boron Nitride-Based Junctions. *Nano Lett.* **2015**, *15*, 7329−33.
(38) Kirkland, E. J. *Advanced Computing in Electron Microscopy*; Springer: 2020.
(39) Fang, S.; Wen, Y.; Allen, C. S.; Ophus, C.; Han, G. G. D.; Kirkland, A. I.; Kaxiras, E.; Warner, J. H. Atomic Electrostatic Maps of 1D Channels in 2D Semiconductors Using 4D Scanning Transmission Electron Microscopy. *Nat. Commun.* **2019**, *10*, 1127.

https://doi.org/10.1021/acs.nanolett.1c01636
Nano Lett. 2021, 21, 7131−7137